NASA Technical Memorandum 106039
ICOMP–93–3

On the Structure of Gaseous Confined Laminar Diffusion Flames/Numerical Investigation

M.A. Mawid
Institute for Computational Mechanics in Propulsion
Lewis Research Center
Cleveland, Ohio

D.L. Bulzan
Lewis Research Center
Cleveland, Ohio

and

S.K. Aggarwal
The University of Illinois at Chicago
Chicago, Illinois

and Institute for Computational Mechanics in Propulsion
Lewis Research Center
Cleveland, Ohio

February 1993

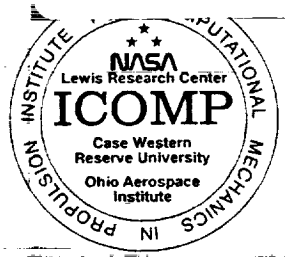

NASA

On the Structure of Gaseous Confined Laminar Diffusion Flames/Numerical Investigation

M.A. Mawid
Institute for Computational Mechanics in Propulsion
NASA Lewis Research Center
Cleveland, Ohio

D.L. Bulzan
NASA Lewis Research Center
Cleveland, Ohio

and

S.K. Aggarwal*
The University of Illinois at Chicago
Chicago, Illinois
and Institute for Computational Mechanics in Propulsion
NASA Lewis Research Center
Cleveland, Ohio

ABSTRACT

The structure and characteristics of gaseous confined laminar diffusion flames are investigated by numerically solving the time-dependent two-dimensional axisymmetric conservation equations. The numerical model accounts for the important chemical and physical processes involved, including axial diffusion, viscous effects, radial convection, and finite-rate chemistry. The numerical results clearly show that the flame has a finite thickness and leakage of fuel vapor into the flame zone is possible. The effect of heat release is found to induce some radial flow. Predicted flame shape and dimensions are compared to the classical Burke-Schumann flame. The numerically calculated flame is observed to be about 15% taller and 5% narrower than that of the Burke-Schumann solution under the same conditions.

*Corresponding Author

INTRODUCTION

Diffusion flames are those types of flames where the fuel and oxidizer are initially separated and combustion is governed by the diffusion of the reactants toward each other. The fundamental processes that control the combustion phenomenon are very complicated and strongly coupled even for simple gaseous diffusion flames. These processes include mixing, chemical reactions, diffusion, flame radiation, soot formation, and buoyancy-generated convection. Fundamental studies of laminar diffusion flames are essential for the understanding of this class of flames and may provide insight into turbulent diffusion flames, which are of greater practical interest and have not been entirely understood.

Burke and Schumann (1928), seven decades ago, presented a theory for laminar gaseous diffusion flames. The apparatus, in which Burke and Schumann produced a gaseous diffusion flame, consisted of two concentric tubes; an inner tube in which the fuel gas flows and on outer tube through which the air flows. When the fuel gas comes in contact with the air, assuming the existence of an ignition source, a flame is established. The theory of diffusion flames proposed by Burke and Schumann contained a number of fundamental assumptions. The important assumptions are that the velocity of fuel and oxidizer is uniform and constant everywhere in the flame zone, mixing of the two gas streams occurs by only radial diffusion, diffusion coefficients of all species are equal and constant, and chemical reaction time scale is very small compared to the diffusion time scale. These assumptions have been justified on the grounds that they render the mathematical treatment of diffusion flames amenable to an analytic solution. Some of these assumptions cannot be reconciled, however, on physical grounds. Consider the first assumption, for example; because of the high temperature developed by the flame and the subsequent expansion of gases, large velocity differences exist at different points along the center line of the two concentric tubes. Moreover, as the mixing time scale is reduced to become comparable to the chemistry time scale (i.e., near extinction), the Burke-Schumann's analysis becomes inapplicable.

A number of studies have followed the Burke-Schumann's analysis in an attempt to reexamine the proposed theory by means of relaxing some of the assumptions and still treating the problem analytically. Clarke (1966, 1967), for instance, investigated the effects of finite

chemistry on the flame characteristics, while retaining the other fundamental assumptions. His results indicated a finite flame zone thickness characterized by steep temperature gradients. The flame height was however found to coincide with that predicted by Burke Schumann solution under the same conditions. An investigation, due to Chang and Law (1984), accounted for the effect of streamwise diffusion in the original Burke-Schumann model. They obtained relatively different flame characteristics such as flame height and shape. Penner et al. (1984) studied the effects of unequal inlet velocities and different diffusion coefficients on the behavior of the flame. They concluded that unequal velocities for the two streams can indeed distort the flame. Further investigations of the Burke-Schumann flame for multiple coupled laminar diffusion flames were undertaken, by Bahadori et al. (1986) and Li et al. (1986) to predict the flames characteristics and shapes.

These studies clearly demonstrate an effort to obtain a more realistic flame structure and better understanding of the various processes involved. Because of the non-linearity and the coupling of fluid mechanics, heat release, chemistry, and mass diffusion processes, an analytic solution for this catergory of diffusion flames cannot be obtained. A detailed solution can only be sought numerically. Gosman et al. (1969) conducted a numerical investigation to simulate laminar jet diffusion flames by solving the two-dimensional steady-state equations but still maintaining some of the Burke-Schumann assumptions such as equal diffusion coefficients, flame sheet model and unity Lewis number. Another numerical study by Mitchell et al. (1980) simulated steady-state-laminar diffusion flames with the flame sheet model. The focus of these numerical studies was to provide some more realistic flame characteristics such as flame height and shape. However, the flame structure, i.e., temperature, concentration, velocity fields and their interaction, and the effects of finite-rate chemistry have not been reported previously.

The objective of the present study is to conduct a detailed numerical investigation, which accounts for the important physical and chemical processes and thus achieve a more fundamental understanding of diffusion flames. In addition, the present work will possibly serve as an instrument by which the severity of the fundamental assumptions such as those made by Burke and Schumann can be assessed. This would also provide guidelines for the validation of the existing analytic models and possibly encourage for further development of these models. As a first step, flame radiation, soot formation, and buoyancy-induced convection effects are not

considered in the present study.

In the present analysis, the unsteady conservation equations for continuity, species, momentum, and energy are solved numerically via the modified KIVA-II computational algorithm of Amsden et. al. (1989). A one-step reaction scheme and an additional three reactions for the predictions of nitric oxides and six equilibrium reactions are used. The results show the existence of large temperature gradients with a finite flame region. The computed flame height for the one-step reaction scheme is about 15% larger than that given by the analytic model.

GOVERNING EQUATIONS

Figure 1 shows a schematic of the physical model considered in the present study. It consisted of two concentric tubes with a mixture of gaseous fuel and nitrogen flowing upward in the inner tube of radius = 0.5 cm, and at the opening AA comes in contact with air that flows through the outer tube of radius R=2 cm. The radial distance is represented by r and the vertical or axial distance, measured from AA, is denoted by z.

The governing equations are written in vector form and the differential operators are referenced to a cartesian coordinate system.

Mass species continuity:

$$\frac{\partial \rho_i}{\partial t} + \vec{\nabla} \cdot (\rho_i \vec{u}) = \vec{\nabla} \cdot (\rho D \vec{\nabla} Y_i) + \dot{\rho}_i^c \qquad (1)$$

where ρ_i is the mass density of species i, Y_i is the mass fraction of species i, $\vec{u}$ the fluid velocity, and $\dot{\rho}_i^c$ the rate of change of ρ_i due to chemical reactions. D is the diffusion coefficient, assumed to be the same for all species, and is related to the fluid viscosity through the Schmidt number as

$$D = \frac{\mu}{\rho S_c}$$

Overall mass continuity:

$$\frac{\partial \rho}{\partial t} + \vec{\nabla} \cdot (\rho \vec{u}) = o \tag{2}$$

Momentum:

$$\frac{\partial (\rho \vec{u})}{\partial t} + \vec{\nabla} \cdot (\rho \vec{u}\vec{u}) = - \vec{\nabla} p + \vec{\nabla} \cdot \underline{\sigma} \tag{3}$$

Here p is the fluid pressure and $\underline{\sigma}$ is the viscous stress tensor expressed as

$$\underline{\sigma} = \mu \left[\vec{\nabla} \vec{u} + (\vec{\nabla} \vec{u})^T \right] + -2/3 \mu \, \vec{\nabla} . \, \vec{u} \, \underline{B}$$

where the superscript T denotes the transpose, and B is the unit dyadic. The Sutherland formula is used for the molecular viscosity of air

$$\mu_a = \frac{A_1 T^{3/2}}{T + A_2}$$

where $A_1 + A_2$ are constants.

Energy:

$$\frac{\partial (\rho I)}{\partial t} + \vec{\nabla} \cdot (\rho \vec{u} I) = -p \, \vec{\nabla} \cdot \vec{u} - \vec{\nabla} \cdot \vec{J} + \dot{Q}_c \tag{4}$$

I is the specific internal energy and $\dot{Q}_c$ is a chemical source term defined later. The heat flux vector $\vec{J}$ is given as

$$\vec{J} = - k \vec{\nabla} T - \rho D \sum_i h_i (\vec{\nabla} y_i)$$

The thermal conductivity k is related to the Prandtl number as

$$k = \frac{\mu C_p}{P_r}$$

Note that the Schmidt and Prandtl number are assumed to be constant. Their values are taken as 1.0 and 0.7 respectively. The equation of state and the state relations are

$$p = R_u \rho T \sum_i Y_i / W_i \tag{5}$$

$$I(T) = \sum_i Y_i I_i (T) \tag{6}$$

$$C_p (T) = \sum_i Y_i C_{pi} (T) \tag{7}$$

and

$$h_i (T) = I_i (T) + R_u T / W_i \tag{8}$$

where R_u is the universal gas constant and w_i is the molecular weight of species i. The values of h_i (T) and C_{pi} (T) are obtained from the JANAF table of Stull and Prophet (1989). The source/sink terms due to chemistry and the reaction rate expressions are given in Appendix A.

Boundary and Initial Conditions:

Refering to Fig. 1, the initial and boundary conditions are given as:

At t = 0.0, $Y_f = 0$, $Y_{02} = 0.23$, $Y_{N2} = 0.77$, T = 400 K

For $0 \le r \le L$, Z = 0

$Y_f = 0.59$, $Y_{02} = 0.0$, $Y_{N2} = 0.41$, and T = 400 K

For $L \le r \le R$, Z = 0

$Y_f = 0$, $Y_{02} = 0.23$, $Y_{N2} = 0.77$, and T = 400 K

For $0 < r < R$, Z = 0

u = 30cm/s, v = 0

For $0 < r < R$, Z = H

$p = p_{atm}$

For $0 \le z \le H$ and r = 0

$$\frac{\partial u}{\partial r} = \frac{\partial v}{\partial r} = \frac{\partial I}{\partial r} = \frac{\partial Y_f}{\partial r} = 0.0$$

For $0 \le z \le H$ and r = R

$$u = v = 0.0,\ T = 400\ K,\ and\ \frac{\partial Y_f}{\partial r} = 0.0$$

Here u and v are the axial and radial velocity components respectively.

NUMERICAL PROCEDURE

The conservation equations of mass species, continuity, momentum, and energy are solved numerically via the KIVA-II computational algorithm of Amsden et al. (1989). The equations

are integrated using the control volume approach. The computational grid is made up of arbitrary shaped hexahedronal cells whose vertices coordinates are referenced with respect to a fixed system of cartesian coordinates and can be either specified to be fixed in space (Eulerian) or moving (Lagrangian). The volume of a hexahedran is computed by dividing it into five tetrahedral and calculating each volume and then summing. A cell surfaces area is found by dividing the surface into four nonplanar triangles and computating each triangle surface area and then adding them up as shown by Pracht (1975).

The computational domain is discretized into a number of finite cells. A block of ten cells, two and five in the radical and axial directions respectively, are assigned to be the ignition source. Ignition energy is deposited in these cells for a certain duration. The amount of ignition energy, duration, and location of the ignition source are determined by numerical experiments in such a way that a flame kernel can be created, leading to a self-sustained combusting situation. Note that the ignition parameters are very critical in deterring the state of the established flame kernel and the resulting combustion wave. For instance, turning off the ignition source before burning becomes self-supported can result in a flame lift-off situation due to thermal losses from the flame kernel.

Two types of coordinate systems for geometrical specifications have been adopted in the literature. In the first, the governing equations are transformed into a generalized orthgonal curvilinear coordinate system. As a result, the physical domain is mapped into a simple computational domain. The metric coefficients resulting from this coordinate transformation can be easily computed using finite difference approximations. The second type is to solve for a given problem in its physical space with reference to a particular coordinate system as is done in KIVA-II. No mapping is required in this case and the equivalent of the metric terms is strictly determined by the principles of geometry. The ten metric quantities required are the three components of each of the three surface areas of a cell together with its volume. Therefore, no global or even local coordinate transformation needs to be specified and the only information needed about the mesh is the three cartesian coordinates of the eight vertices of every cell.

It is understood that the KIVA-II computer code was written particularly for moving computational grids, i.e., internal combustion engines, although it contains an option for inflow

and outflow boundary conditions. The implementation of inflow and outflow boundary conditions must be done very carefully, however, since the outflow boundary conditions can pose a problem for low-speed elliptic computations such as those considered here. This is because a slightly improper prescription or treatment of that boundary may result in pressure signals sent back into the computational domain which greatly affects the entire upstream flow. The original KIVA-II algorithm, was found to be sensitive to these pressure waves which precluded the attainment of a steady state solution. KIVA-II uses a staggered grid where the fundamental velocities and the thermodynamic quantities are located at the cells vertices and centers respectively. In addition to the vertex-centered velocities, cell face centered velocities are also employed to calculate cell volume changes and material volume fluxes across cell faces. The cell face based velocities differ from those of the fundamental ones only by the viscous term. In differencing the equation for the cell face centered velocities, it is suggested that the atmospheric pressure be imposed at some distance above the outflow boundary, see Eq. (86) of the report by Amsden et al. (1989). However, in integrating the momentum equation for the fundamental velocities, the pressure forces acting on the outlet boundary from the outside (i.e., on the momentum cell faces lying exactly on the outflow boundary) were not accounted for. In general, this results in decoupling of the velocity and pressure fields for the boundary vertices. It is important to note here that convergence of the pressure field is obtained using the cell face-based velocities where the effect of the pressure at the outflow boundary is accounted for. In the modified version, the pressure field is added to the fundamental velocities as pressure forces acting on the momentum cell faces after the pressure field is converged.

A total residual criterion in the velocity field for checking the attainment of a steady-state solution was used and the results, before and after accounting for the effects of the pressure forces, are shown in Fig. 2. While the original KIVA-II predictions showed continuous oscillation, the addition of the pressure forces to the algorithm clearly exhibits the attainment of a steady-state solution for a specified pressure convergence tolerance. Note that the pressure forces are imposed at some distance above the physical boundary. The optimum distance, yielding results largely free of reflected pressure waves, was determined by numerical experiments and was found to be about 3.5 times the average axial cell size.

Since KIVA-II solves the finite difference approximations of a given problem in its

physical space, (i.e., no mapping is required) the two-dimensional axisymmetric computations are carried out in a cylindrical sector, referenced with respect to the x, y, and z cartesian coordinates, and whose front and back boundary conditions are periodic. The computational grid employed in this study is shown in Fig. 3 and consisted of 50 x 75 cells which yielded results that are grid-size independent. The temporal step size used here varied from 10^{-5} to 10^{-6}s. Finally, the CPU time needed to obtain a steady-state solution was about 9-10 hours on a the Cray-YMP.

RESULTS AND DISCUSSIONS

The fuel selected for this study is gaseous n-octane. The parameters used for the one-step reaction and ten-step reaction schemes are given in Appendix A. The computations are reported for overall stoichiometric conditions. Results for the one-step scheme are presented first.

One Step Reaction Scheme:

The global structural features of the steady-state diffusion flame at a physical time of 0.68 s, are shown in Fig. 4(a-c). The z coordinate is along the axis of symmetry and the r coordinate is along the radial direction. It can be seen that large temperature gradients exist, see Fig. 4a, ranging from 500 K to 1900 K contours and spanning across the entire flow field. The maximum temperature contour is seen to occur towards the oxidizer side, in a region where the fuel and oxidizer are nearly in stoichiometric proportions. The fuel and oxygen mass fraction contours show some mixing of the fuel and oxidizer species near the inflow boundary. In fact, it is seen that while the fuel species diffuses radially, the oxygen species appears to recede toward the combustor wall and combustion lies on the oxygen side. The fuel species maintains a significant radial diffusion to the extent that it axially diffuses. The coexistence of the fuel and oxygen species, even in regions where intense combustion is taking place, indicates that the flame has a finite thickness. This is further demonstrated in the temperature contours, i.e., large temperature gradients. Note that the maximum computed temperature is 2020 K. The temperature changes at the exit are due to the outflow boundary condition and will be discussed later.

The fuel mass fraction contours, Fig. 4b, show that some fuel flows out of the combustor.

The oxygen mass fraction contours, Fig. 4c, indicate that all the oxygen flowing into the combustor is consumed. The leakage of fuel through the flame, which is probably due to the large velocities induced by the flame, further demonstrates that the gaseous diffusion flame possesses a finite flame thickness and the flame zone never collapses onto a surface due to the finite reaction rate. This is in contrast to the result given by the flame sheet model.

The existence of a temperature distribution and the presence of fuel within the reaction zone precludes a clear definition of a flame shape. Burke and Schumann, for example, defined the flame front at the location where the concentrations of the reactants are zero. In the present investigation, due to the finite-rate chemical reaction, the flame front is defined to be the location where the maximum temperature occurs in each radial row of cells along the combustor where oxygen is still present. By connecting these points, the flame shape and dimensions are obtained as shown in Fig. 5.

To assess the importance of numerically predicted flame shape and dimensions, the classical Burke-Schumann analysis is used to reproduce the flame shape and height for the same boundary conditions, stoichiometry, and fuel type as those used in the computations. As indicated in Fig. 5, two major differences appear to exist between the numerically calculated flame and the analytical solution. First of all, the analytical flame is wider than the computed one and exhibits a very smooth flame front compared to the computed flame. The slight variations in the computed flame front location are believed to be caused by the approach used in defining the flame front. Note that other definitions, such as the location of the 5% or 1% of the normalized fuel mass fraction are possible. Since the predicted flame structure indicates the presence of fuel in the intense burning region, this widens the reaction zone and is believed to contribute largely to the width difference. Secondly, the computed flame is about 16% taller than the analytic one. A plausible explanation is that axial diffusion and the increase in the axial gas velocity because of the temperature rise in the flame, are responsible for these differences, since these effects were not considered in the Burke Schumann's analysis.

In order to further show the effect of heat release on the computed flame height, the predicted velocity vectors are plotted in Fig. 6. The velocity vectors show an increase in magnitude due to the heat release and associated expansion of the gas. The maximum velocities

are found near the exit of the computational domain. The velocity vectors show a dominant axial flow with the exception of a region adjacent to the outflow boundary, where the combustion products appear to flow towards the center line. It is believed that this behavior is caused by the outflow pressure condition. In the present analysis, no attempt was made to entirely prevent the reflection of pressure waves from the outflow boundary. This is important for very low-speed calculations such as those in the present investigation, where the upstream mach number is about 8×10^{-4}. These reflected waves do not propagate upstream and thus appear to have only a slight effect on the predicted flame behavior. This is clearly demonstrated in the velocity vectors, Fig. 6.

Ten Step Reaction Scheme

Since the computations with the one-step reaction scheme indicate relatively high temperatures (maximum temperature is 2020 K), it is postulated that equilibrium reactions may be occurring along with the kinetic reactions. In this study, the fuel oxidation is still assumed to be governed by a one-step reaction, i.e., the products are $C0_2$ and H_20. However, as the temperature field develops, the composition field also changes due to the equilibrium reactions, since the equilibrium reaction rates are only temperature dependent. Note that reactions 2, 3, and 4, which are kinetic (see Appendix I), are for the prediction of nitric oxides and are not relevant to the present study. In the following discussion, the one and ten step reaction schemes are referred to as schemes 1 and 2 respectively, and the influence of the equilibrium reactions on the flame structure is assessed.

Fig. 7(a-c) shows the steady state flame structure for scheme 2 at the same physical time, t=0.68s, as that of scheme 1. The qualitative features are seen to be essentially similar to those with scheme 1, presented in Figs. 4-6. Quantitatively, however, there are differences. The size of the 1500 K contor for scheme 2 is significantly smaller than that of scheme 1, see Figs. 4a and 7a. The size of the 1700 K contour for scheme 2 is also smaller than that contour for scheme 1. Furthermore, the 1500 K contour extends from about z=4 to 8.8 cm along the center line for scheme 1, whereas for scheme 2, it extends from z=5.3 to 6.3 cm. A similar behavior is observed in the 1300 K contours. These differences indicate that the region of intense reaction

is relatively smaller for scheme 2 compared to that for scheme 1.

The effect of employing equilibrium reactions is further observed in the oxygen mass fraction contours. While all the oxygen flowing into the combustor is consumed, some oxygen is present at larger axial distances for scheme 1 as indicated by the 0.03 and 0.05 contours. This further supports the earlier observation regarding the decrease in the size of intense burning region. The fuel mass fraction contours also exhibit some differences for the two schemes. The 0.10 contour, for instance, extends to about z=4.5 cm along the center line for scheme 1, while for scheme 2, it reaches z=5 cm, indicating the difference in the burning zone location and size for the two schemes.

Fig. 8 shows the diffusion flame shapes predicted by the one-reaction and ten-reaction schemes. As indicated, the flame shapes are almost identical for the two schemes. Note, however, that these flames have slightly different temperature values since the flame shape is determined by the location of the maximum temperature. In addition, there is some difference in the flame heights for the two schemes. This is a direct consequence of the modified flame structure resulting from the inclusion of the equilibrium reactions.

The velocity vector distribution in the combustor at steady state (t=0.68s) for scheme 2 is shown in Fig. 9. The velocity vectors for scheme 2 (Fig. 9) are qualitatively similar to those for scheme 1 (Fig. 6). The velocity vectors clearly illustrate the influence of the heat release, through significant variations vector magnitudes. This effect of heat release is not considered in the classical diffusion flame analysis. Note also, that the maximum velocity occurs near the combustor exit, as noted earlier for the one-reaction scheme.

CONCLUSION

The structure of laminar confined gaseous diffusion flames is studied numerically by solving the time-dependent two-dimensional axisymmetric conservation equations via the KIVA-II computational algorithm. The original treatment of the outflow boundary condition in the numerical algorithm is modified to achieve a steady-state solution for a very low-speed flow. A one-step finite-rate reaction scheme for the hydrocarbon fuel with six equilibrium reactions is

employed for this study. The predictions show some influence of the downstream pressure boundary condition near the exit, but results near the flame zone do not appear to be affected.

The numerical results clearly indicate the existence of sharp temperature gradients across the flowfield and the flame is found to possess a finite thickness as opposed to the classical Burke-Schumann flame. The computations also predict that fuel and oxygen can coexist in regions of the flow field where the burning is not intense. Some radial flow is predicted as a result of the gas expansion due to heat release, indicating that some mixing also occurs by radial convection in addition to radial diffusion.

In this study, the flame front location is defined by the location of the maximum temperature in each row of cells in the computational domain. The comparison of the numerically computed flame shape and dimensions with those of the Burke Schumann flame under the same conditions shows that the computed flame is about 15% taller and 5% narrower. The computed flame shape, particularly the shape of the flame peak, was found to be in good agreement with that observed experimentally by Burke and Schumann (1928).

The flame structure is found to be mildly sensitive to the two reaction schemes employed. The inclusion of six equilibrium reactions with the single finite-rate reaction reduces the maximum temperature by about four percent compared to the single reaction alone. In addition, the reactant mass fraction distributions also show some sensitivity to the reaction schemes. For the one-step scheme without equilibrium reactions, the oxygen is completely consumed in the combustor. However, with the equilibrium reactions included, some oxygen flows out of the combustor.

ACKNOWLEDGEMENT

This study has been supported by the NASA Lewis Research Center and by the Institute of Computational Mechanics in Propulsion, Cleveland, Ohio. Some of the computations have been performed on Cray-YMP at the NCSA, University of Illinois at Urbana-Champaign.

NOMENCLATURE

A	Pre-exponential factor in the reaction rate expression
c_{pi}	Specific heat for the ith species
D	Diffusion coefficient
E	Activation energy
h_i	Enthalpy of the ith species
I	Internal energy
k	Thermal conductivity
p	Pressure
r	Radial coordinate
R_u	Universal gas constant
t	Time
T	Temperature
v	Radial gas velocity
u	Axial gas velocity
W_{av}	Average molecular weight excluding fuel vapor
W_i	Molecular weight of the ith species
Y_i	Mass fraction of the ith species
z	Axial coordinate
μ	Viscosity
ν_i	Stoichiometric coefficient
ρ	Density

Subscripts

a	Air
f	Fuel
i	species
o	Oxidizer

REFERENCES

1. Burke, S.P.; and Schumann, T.E.W.: Diffusion Flames. Ind. Eng. Chem., vol. 20, no. 10, 1928, pp. 998-1057.

2. Clarke, J.F.: Hydrogen Diffusion Flames. J. Inst. Math. Its Appl., vol. 3, 1967, pp. 347-354.

3. Clarke, J.F.: Equilibrium Chemistry-Diffusion Flames. Proc. R. Soc. London A., vol. 307, 1968, pp. 283-302.

4. Chang, S.H.; and Law, C.K.: Streamwise Effects on Diffusion Flames. Combust. Sci. Technol., vol. 37, 1984, pp. 21-46.

5. Penner, S.S; Bahadori, M.Y.; and Kennedy, E.M.: Effects of Variable Diffusion Coefficients on Burke-Schumann Flames. Dynamics of Flames and Reactive Systems, Progress in Astronautics and Aeronautics, vol. 95, J.R. Bowen, ed., AIAA, New York, 1984, pp. 262-269.

6. Bahadori, M.Y.; Li, C.-P.; and Penner, S.S.: Two Adjacent, Coupled Laminar Diffusion Flames with Cylinderical Symmetry. Dynamics of Reactive Systems. Pt. 1: Flames and Configurations, Progress in Astronautics and Aeronautics, vol. 105, J.R. Bowen, J.-C. Leyer, and R.I. Soloukhin, eds., AIAA, New York, 1986, pp. 192-207.

7. Li., G.P.; Wiesenhann, D.; and Penner, S.S.: Coupled Laminar Diffusion Flame with Variable Properties. Combust. Flame, vol. 65, 1986, pp. 215-225.

8. Gosman, A.D., et al.: Heat and Mass Transfer in Recirculating Flows, Academic Press, New York, 1969.

9. Mitchell, R.E., Sarofim, A.F.; and Clomburg, L.A.: Experimental and Numerical Investigation of Confined Laminar Diffusion Flames. Combust. Flame, vol. 37, 1980, pp. 227-244.

10. Amsden, A.A.; O'Rourke, P.J.; and Butler, T.O.: KIVA-II: A Computer Program for Chemically Reactive Flows with Fuel Sprays. Report LA-11560-MS, Los Alamos National Laboratory, NM, 1989.

11. Stull, D.R.; Prophet, H.; and Chase, M.W.: JANAF Thermochemical Tables. Third ed. American Chemical Society, Washington, DC, 1986.

12. Pracht, W.E.: Calculating Three-Dimensional Fluid Flows at All Speeds with an Eulerian-Lagrangian Computing Mesh. J. Comput. Phys., vol. 17, Feb. 1975, pp. 132-159.

Appendix A

The octane fuel reaction is assumed to be governed by a irreversible global one-step scheme of the form:

$$C_8 H_{18} + 12.5\ 02 \rightarrow 8\ CO_2 + 9\ H_20 \qquad \text{(A-1)}$$

Nitric oxide (NO) formation is modeled through the extended Zeldovich scheme as:

$$0 + N_2 \longleftrightarrow N + N0 \qquad \text{(A-2)}$$

$$0 + N0 \longleftrightarrow 0_2 + N \qquad \text{(A-3)}$$

$$N + OH \longleftrightarrow H + N0 \qquad \text{(A-4)}$$

Reactions (A-1) through (A-4) are kinetic ones and their global reaction rate expression is given as

$$\dot{\omega} = K_{fr} \prod_i \left(\frac{\rho_i}{W_i}\right)^a - k_{br} \prod_i \left(\frac{\rho_i}{W_i}\right)^b \qquad \text{(A-5)}$$

where a and b are the reaction orders. The forward and backward reaction rate constants, K_{fr} and K_{br}, are determined from the Arrhenius expression as

$$K_{fr,\,br} = A\ exp\ (-\ E/R_u T)$$

The six equilibrium reactions considered here are

$$H_2 \longleftrightarrow 2H \qquad \text{(A-6)}$$

$$O_2 \longleftrightarrow 20 \qquad \text{(A-7)}$$

$$N_2 \longleftrightarrow 2N \qquad \text{(A-8)}$$

$$0_2 + H_2 \longleftrightarrow 20H \qquad \text{(A-9)}$$

$$0_2 + 2H_20 \longleftrightarrow 40H \qquad \text{(A-10)}$$

$$0_2 + 2C0 \longleftrightarrow 2CO_2 \qquad \text{(A-11)}$$

The rate of each equilibrium reaction is given by

$$\prod_i (\rho_i/W_i)^{\nu_i'' - \nu_i'} = K_c(T)$$

where $K_c(T)$ is the concentration equilibrium constant and ν_i' and ν_i'' are the stoichoimetric coefficients of species i on the left and right side of each reaction.

The chemical source terms in the species continuity and the energy equations are respectively given by

$$\dot{\rho}_i^c = W_i \sum_r (\nu_i'' - \nu_i') \dot{\omega}$$

$$\dot{Q}^c = \sum_r \sum_i (\nu_i' - \nu_i'') (\Delta h_f^\circ)_i \dot{\omega}$$

where $\dot{\omega}$ is given by equation A-5. $(\Delta h_f^\circ)_i$ is the heat of formation of species i and the values are taken from JANAF table compiled by Stull and Prophet (1989). Finally, the activation energy and preexponential factor for reaction (A-1) are respectively E = 25.6 kcal/mole and A = 10^{12}.

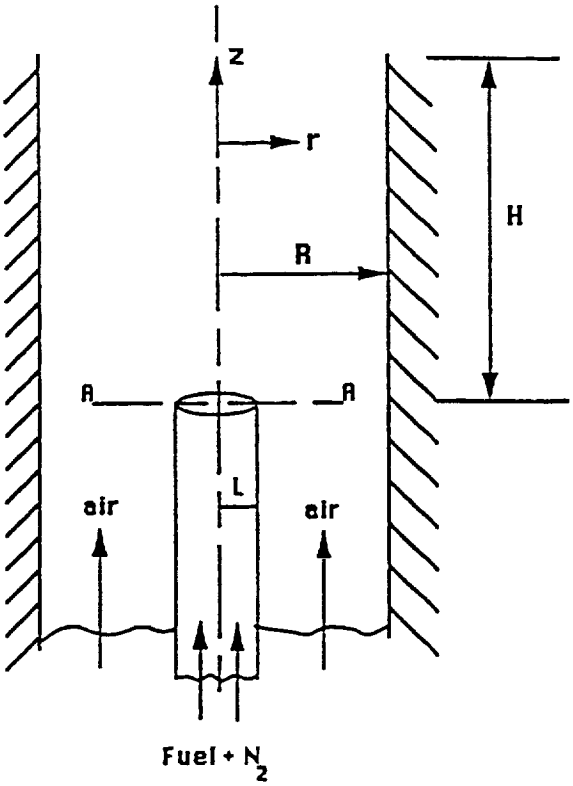

Figure 1.—Schematic of the physical model.

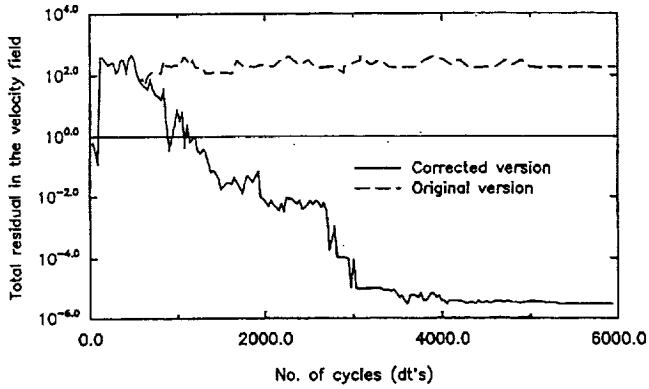

Figure 2.—Total residual in the velocity field predicted by the original and corrected KIVA-II codes.

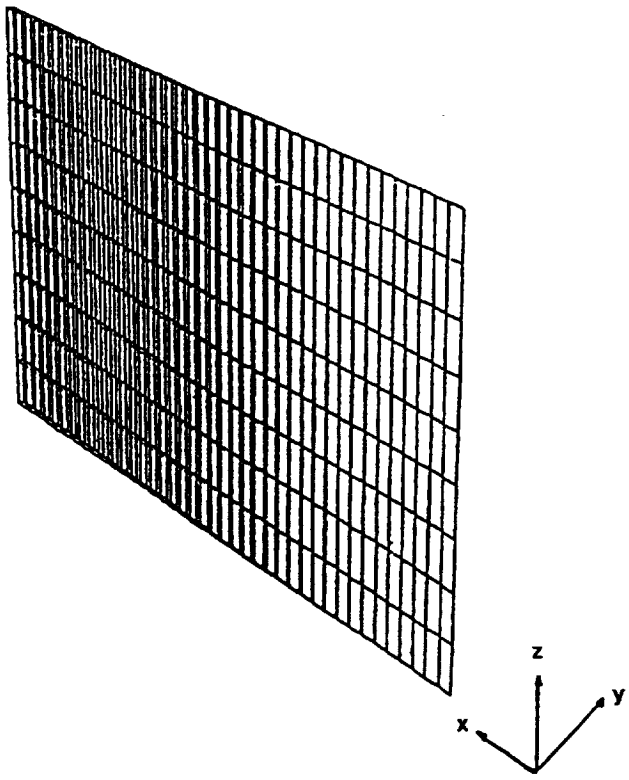

Figure 3.—The computational grid.

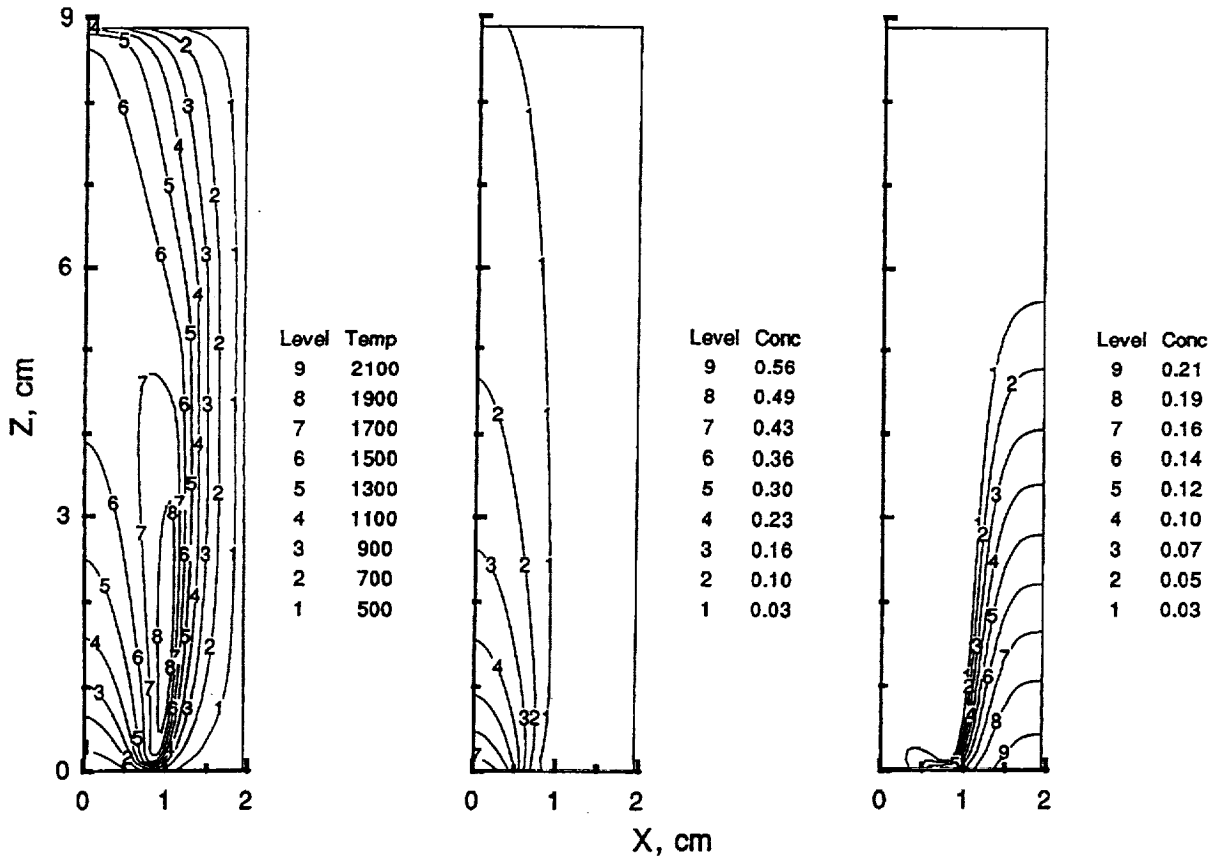

(a) Temperature contours. (b) Fuel mass fraction contours. (c) Oxygen mass fraction contours.

Figure 4.—Gaseous diffusion flame at time = 0.68 s.

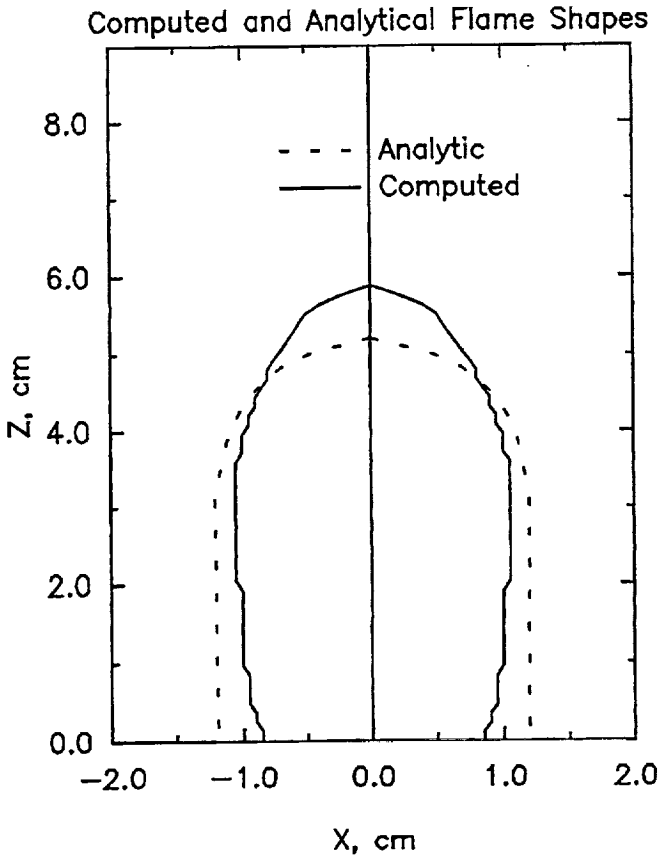

Figure 5.—Comparison of the computed and the analytical gaseous diffusion flame shape.

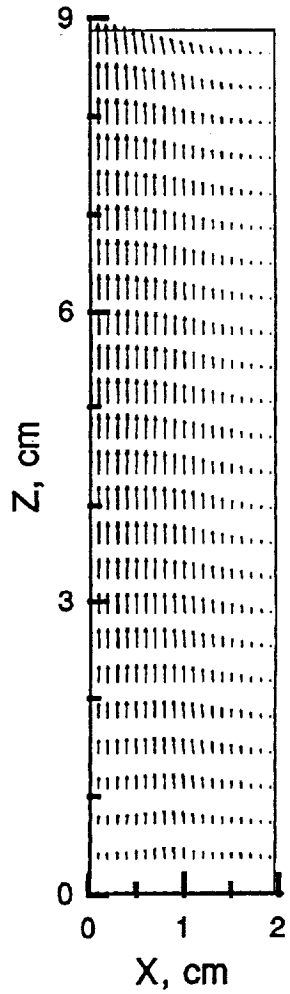

Figure 6.—Velocity vector distribution for the one-reaction scheme at time = 0.68 s.

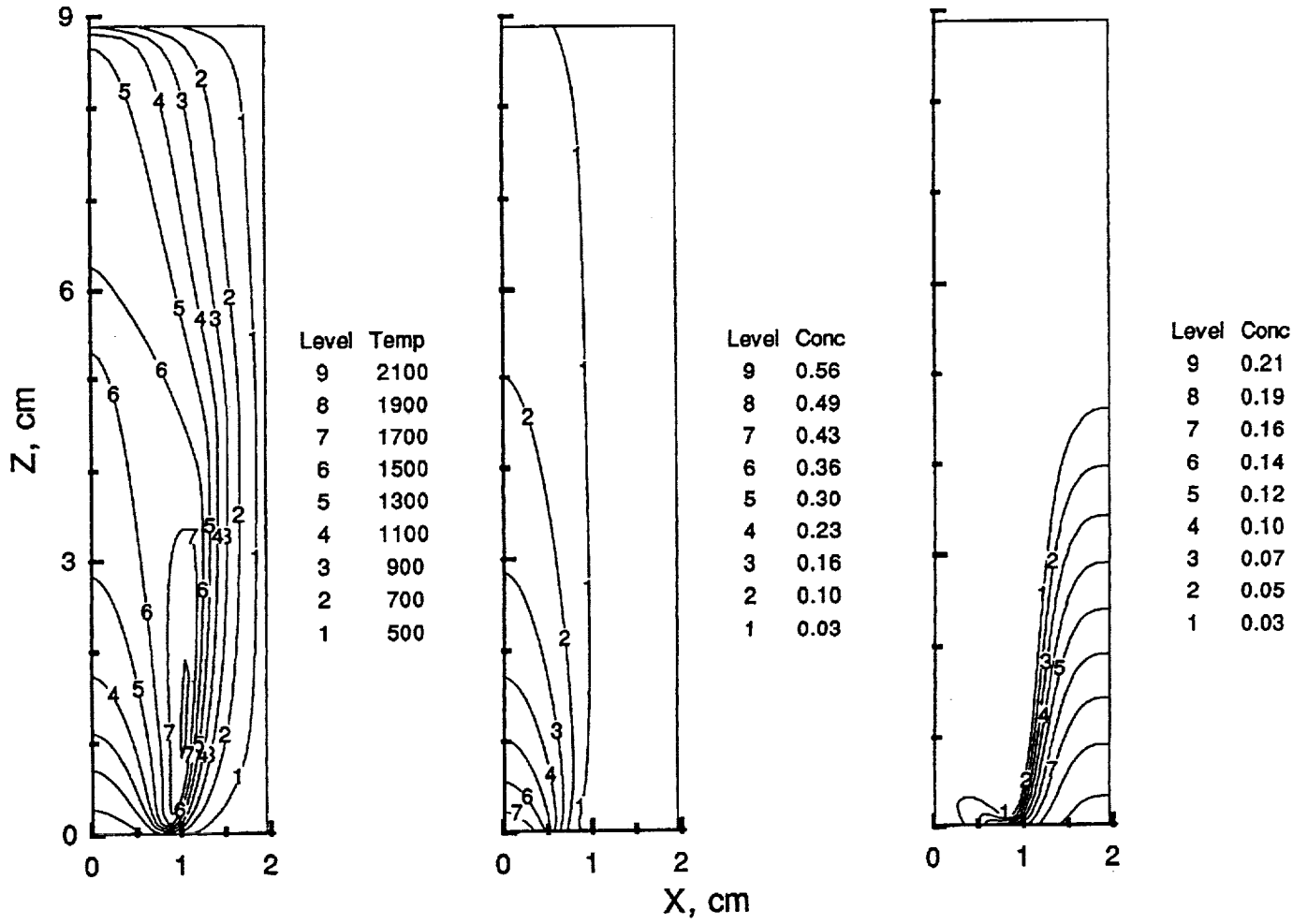

(a) Temperature contours. (b) Fuel mass fraction contours. (c) Oxygen mass fraction contours.

Figure 7.—Gaseous diffusion flame with 10 reactions at time = 0.68 s.

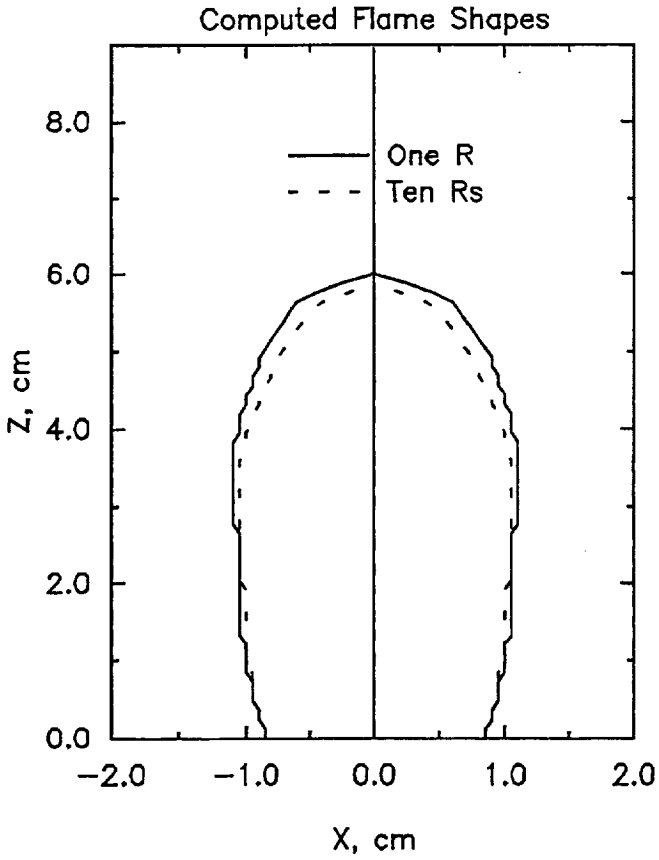

Figure 8.—Diffusion flame shapes predicted by one-reaction and ten-reaction schemes.

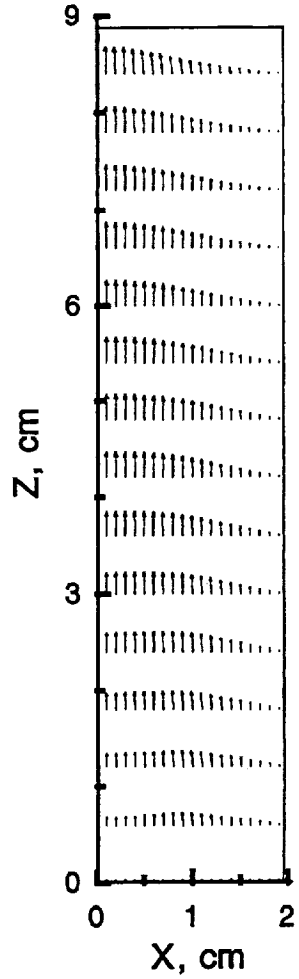

Figure 9.—Velocity vector distribution for the ten-reaction scheme at time = 0.68 s.

REPORT DOCUMENTATION PAGE

Form Approved
OMB No. 0704-0188

1. AGENCY USE ONLY (*Leave blank*)	2. REPORT DATE	3. REPORT TYPE AND DATES COVERED
	February 1993	Technical Memorandum

4. TITLE AND SUBTITLE
On the Structure of Gaseous Confined Laminar Diffusion Flames/Numerical Investigation

5. FUNDING NUMBERS
WU-505-62-21

6. AUTHOR(S)
M.A. Mawid, D.L. Bulzan, and S.K. Aggarwal

7. PERFORMING ORGANIZATION NAME(S) AND ADDRESS(ES)
National Aeronautics and Space Administration
Lewis Research Center
Cleveland, Ohio 44135-3191

8. PERFORMING ORGANIZATION REPORT NUMBER
E-7613

9. SPONSORING/MONITORING AGENCY NAMES(S) AND ADDRESS(ES)
National Aeronautics and Space Administration
Washington, D.C. 20546-0001

10. SPONSORING/MONITORING AGENCY REPORT NUMBER
NASA TM-106039
ICOMP-93-3

11. SUPPLEMENTARY NOTES
M.A. Mawid, Institute for Computational Mechanics in Propulsion, NASA Lewis Research Center (work funded under NASA Cooperative Agreement NCC3-233). ICOMP Program Director, Louis A. Povinelli, (216) 433-5818; D.L. Bulzan, NASA Lewis Research Center and S.K. Aggarwal, The University of Illinois at Chicago, Chicago, Illinois 60680 and Institute for Computational Mechanics in Propulsion, NASA Lewis Research Center, Cleveland, Ohio (work funded under NASA Cooperative Agreement NCC3-233). Responsible person, M.A. Mawid, (216) 433-5965.

12a. DISTRIBUTION/AVAILABILITY STATEMENT
Unclassified - Unlimited
Subject Category 34

12b. DISTRIBUTION CODE

13. ABSTRACT (*Maximum 200 words*)

The structure and characteristics of gaseous confined laminar diffusion flames are investigated by numerically solving the time-dependent two-dimensional axisymmetric conservation equations. The numerical model accounts for the important chemical and physical processes involved, including axial diffusion, viscous effects, radial convection, and finite-rate chemistry. The numerical results clearly show that the flame has a finite thickness and leakage of fuel vapor into the flame zone is possible. The effect of heat release is found to induce some radial flow. Predicted flame shape and dimensions are compared to the classical Burke-Schumann flame. The numerically calculated flame is observed to be about 15 percent taller and 5 percent narrower than that of the Burke-Schumann solution under the same conditions.

14. SUBJECT TERMS	15. NUMBER OF PAGES
Structure of gaseous diffusion flames; A numerical study	24
	16. PRICE CODE: A03

17. SECURITY CLASSIFICATION OF REPORT	18. SECURITY CLASSIFICATION OF THIS PAGE	19. SECURITY CLASSIFICATION OF ABSTRACT	20. LIMITATION OF ABSTRACT
Unclassified	Unclassified	Unclassified	